Folded dipole plasmonic resonators

K. Choonee[*] and R. R. A. Syms

Optical and Semiconductor Devices group, EEE Department, Imperial College London, Exhibition Road, London SW7 2AZ, UK

[*]*kaushal.choonee@imperial.ac.uk*

Abstract: A class of folded ordered plasmonic dipole nanoresonators based on insulator-metal-insulator (IMI) slab waveguides is proposed and studied. This work is motivated by the development of a novel fabrication process that avoids the need for direct write nanolithography and instead relies on accessible UV lithography and other top-down parallel fabrication techniques that result in metallic dolmen structures with nanometre sized gaps. In this context, the dolmen geometry consists of two vertical segments supporting a flat horizontal slab. It is shown using frequency domain finite element analysis that such structures, which are essentially folded dipole antennas, resonate in a similar manner to their linear unfolded counterparts. The effect of the likely fabrication features is also studied.

OCIS codes: (250.5403) Plasmonics; (240.6680) Surface plasmons; (220.4241) Nanostructure fabrication; (230.5750) Resonators.

References and links

1. S. A. Maier, *Plasmonics: Fundamentals and Applications* (Springer Science, 2007).
2. J. Homola, *Surface Plasmon Resonance Based Sensors* (Springer, 2006), Vol. 4.
3. E. Ozbay, "Plasmonics: merging photonics and electronics at nanoscale dimensions," Science **311**(5758), 189–193 (2006).
4. L. Novotny, R. X. Bian, and X. S. Xie, "Theory of nanometric optical tweezers," Phys. Rev. Lett. **79**(4), 645–648 (1997).
5. P. Nagpal, N. C. Lindquist, S.-H. Oh, and D. J. Norris, "Ultrasmooth patterned metals for plasmonics and metamaterials," Science **325**(5940), 594–597 (2009).
6. G. H. Chan, J. Zhao, E. M. Hicks, G. C. Schatz, and R. P. Van Duyne, "Plasmonic properties of copper nanoparticles fabricated by nanosphere lithography," Nano Lett. **7**(7), 1947–1952 (2007).
7. M. Green and F. M. Liu, "SERS substrates fabricated by island lithography: the silver/pyridine system," J. Phys. Chem. B **107**(47), 13015–13021 (2003).
8. J. Henzie, J. Lee, M. H. Lee, W. Hasan, and T. W. Odom, "Nanofabrication of plasmonic structures," Annu. Rev. Phys. Chem. **60**(1), 147–165 (2009).
9. A. V. Kabashin, P. Evans, S. Pastkovsky, W. Hendren, G. A. Wurtz, R. Atkinson, R. Pollard, V. A. Podolskiy, and A. V. Zayats, "Plasmonic nanorod metamaterials for biosensing," Nat. Mater. **8**(11), 867–871 (2009).
10. N. C. Lindquist, P. Nagpal, K. M. McPeak, D. J. Norris, and S. H. Oh, "Engineering metallic nanostructures for plasmonics and nanophotonics," Rep. Prog. Phys. **75**(3), 036501 (2012).
11. R. R. A. Syms, "Sub-micron structuring at mesa edges," Microelectron. Eng. **73–74**, 295–300 (2004).
12. Y.-K. Choi, J. Zhu, J. Grunes, J. Bokor, and G. A. Somorjai, "Fabrication of sub-10-nm silicon nanowire arrays by size reduction lithography," J. Phys. Chem. B **107**(15), 3340–3343 (2003).
13. T. A. Milligan, *Modern Antenna Design* (Wiley-IEEE Press, 2005).
14. L. Novotny, "Effective wavelength scaling for optical antennas," Phys. Rev. Lett. **98**(26), 266802 (2007).
15. T. Søndergaard and S. I. Bozhevolnyi, "Metal nano-strip optical resonators," Opt. Express **15**(7), 4198–4204 (2007).
16. L. Novotny and B. Hecht, *Principles of Nano-Optics* (Cambridge University Press, 2006).
17. E. N. Economou, "Surface plasmons in thin films," Phys. Rev. **182**(2), 539–554 (1969).
18. T. Søndergaard and S. Bozhevolnyi, "Slow-plasmon resonant nanostructures: Scattering and field enhancements," Phys. Rev. B **75**(7), 073402–073406 (2007).
19. Comsol Multiphysics, Available: http://www.comsol.com/
20. E. M. Hicks, S. Zou, G. C. Schatz, K. G. Spears, R. P. Van Duyne, L. Gunnarsson, T. Rindzevicius, B. Kasemo, and M. Käll, "Controlling Plasmon Line Shapes through Diffractive Coupling in Linear Arrays of Cylindrical Nanoparticles Fabricated by Electron Beam Lithography," Nano Lett. **5**(6), 1065–1070 (2005).
21. M. A. Ordal, L. L. Long, R. J. Bell, S. E. Bell, R. R. Bell, R. W. Alexander, Jr., and C. A. Ward, "Optical properties of the metals Al, Co, Cu, Au, Fe, Pb, Ni, Pd, Pt, Ag, Ti, and W in the infrared and far infrared," Appl. Opt. **22**(7), 1099–20 (1983).

#195436 - $15.00 USD Received 7 Aug 2013; revised 13 Sep 2013; accepted 16 Sep 2013; published 22 Oct 2013

22. T. Siegfried, Y. Ekinci, O. J. F. Martin, and H. Sigg, "Engineering metal adhesion layers that do not deteriorate plasmon resonances," ACS Nano **7**(3), 2751–2757 (2013).
23. D. Punj, M. Mivelle, S. B. Moparthi, T. S. van Zanten, H. Rigneault, N. F. van Hulst, M. F. García-Parajó, and J. Wenger, "A plasmonic 'antenna-in-box' platform for enhanced single-molecule analysis at micromolar concentrations," Nat. Nanotechnol. **8**(7), 512–516 (2013).

1. Introduction

Surface plasmon polaritons (SPP) are bound electromagnetic waves that propagate along metal-dielectric interfaces such as a semi-infinite plane interface [1]. When metallic nanoparticles are considered, charge density oscillations within the metal at characteristic frequencies lead to resonant modes known as localised surface plasmon resonances (LSPRs). Plasmonic resonators have received considerable attention in recent years due to their ability to confine electromagnetic energy to subwavelength scales and their numerous applications in areas such as sensing [2], ultra compact photonic circuits [3], or manipulation of nanoparticles [4] amongst others. All of these applications require the fabrication of optical resonators with nanometre resolution and typically direct-write techniques such as electron beam lithography (EBL) and focussed-ion beam (FIB) machining (see e.g [5].) are used. Whilst precise, such techniques suffer in terms of accessibility and the serial nature limits the area that can be patterned reliably. To overcome this, alternatives such as island and nanosphere lithography [6, 7], soft lithography [8] or electrochemical methods [9] have been proposed (see e.g [10]. for a review of such methods). Despite the large array of tools, reproducibility and uniformity over a large area remains a challenge.

In this work, we propose a new class of plasmonic optical resonators that can be fabricated reliably over large areas by avoiding nanolithography and other serial methods. This method relies on two key features: the angular dependence of the etch rate of some metals under ion beam bombardment, and the use of sidewall processing.

The angular dependence of ion beam etching is discussed in [11], and its suitability for etching nano-gaps in metals is illustrated in Fig. 1(a). The starting point is a Si mesa covered with a SiO_2 layer, which has a finite radius of curvature at the edges. The latter is sputter coated with a conformal layer of a suitable metal and subsequently bombarded by a vertical ion beam in a parallel plate plasma chamber. Metal segments on the curved mesa edge that are tilted with respect to the vertical ion beam are preferentially eroded and this property can be used to form nano-gaps between the horizontal and vertical metal sections (Fig. 1(a)). The gap width is defined by the etch time, plasma power, DC bias and the radius of curvature. Sharper edges, and hence smaller gaps, (of the order of a few nanometres) can be obtained by exploiting anisotropic etching of crystalline Si where the edges are defined by the intersection of the crystal planes.

Sidewall processing exploits processes like reactive ion etching, thermal oxidation, and sputter deposition to define the critical dimensions and optical UV lithography to define larger features like the spacing. A possible approach derived from [12] is illustrated in Fig. 1(b) where the starting point is a micrometre sized Si mesa formed by conventional patterning and etching of a polycrystalline Si (poly-Si) that has been deposited on an oxidised single crystal Si wafer by chemical vapour deposition. The oxide layer acts both as an etch stop to ensure a planar surface and as a mask to pattern the single crystal Si. The poly-Si is first coated conformally with a suitable metal by sputter deposition, and the horizontal facing metal is then removed by an anisotropic etch step. The exposed poly-Si is subsequently removed and the remaining metallic sidewall is used as a mask to pattern the oxide layer. Finally, the oxide pattern is transferred to the underlying Si substrate by a vertical etch and the resulting nanoscale mesa structure can be used as the basic foundation for the edge structuring process illustrated in Fig. 1(a). Note that one critical dimension, the width of the nano-mesa, is defined by the thickness of the deposited metal in the conformal coating process, while the other, the height, is defined by the thickness of the original poly-Si mesa. Also, these steps can be extended to other materials. Fabrication schemes based on the general flow described above are therefore suitable for generating nanometre sized metallic structures resembling dolmens in a reliable manner over a very large area. In archeology, a

#195436 - $15.00 USD Received 7 Aug 2013; revised 13 Sep 2013; accepted 16 Sep 2013; published 22 Oct 2013

dolmen refers to a megalithic tomb constructed as a portal consisting of two upright stones supporting a horizontal one. In this context, the dolmen structure consists of a horizontal metallic segment supported by two vertical segments and separated by nano-gaps. Key geometries and their operation are studied in the next section.

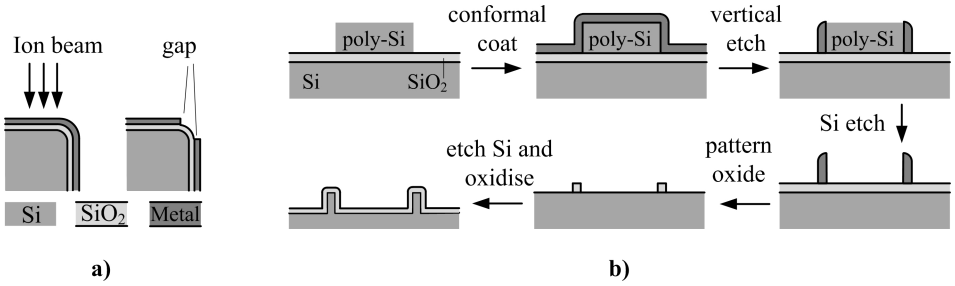

Fig. 1. a) Illustration of nano gaps formed by ion beam etching at mesa edges. b) Proposed process flow exploiting sidewall processing to generate nano-mesa for ion beam edge structuring.

2. Antenna concept and design

The metallic segments separated by nano-gaps described above are effectively insulator-metal-insulator (IMI) slabs of finite length and can behave as optical resonators. If they are considered as isolated single segment rods, by analogy to conventional dipole antennas [13], they are expected to sustain standing waves and resonate when the antenna length, $L = m\lambda_{eff}/2$, where $m = 1, 2\ldots$. Here, λ_{eff} represents an effective wavelength, rather that the excitation wavelength (λ_0), which accounts for the fact the excited wave is strongly bound to the metal [14]. The proposed antenna also exploits elements from so called nano-strip antennas [15] by introducing a subwavelength gap within the dipole, similar to the feed gap in classical half-wave antennas [13], or by placing two or more dipole resonators very close to each other. Both configurations can exhibit large field enhancements in the gap and at the ends. The latter resonators are also called coupled-dipole antennas, and as described in [16], additional degrees of freedom and hence resonant modes can arise. However, in this work, only the field enhancing aspect will be considered.

Symmetric IMI waveguides can sustain two types of propagating waves; a symmetric and an anti-symmetric (also known as a long range SPP) modes [1, 17]. According to [18], only the symmetric mode forms a standing wave on the metal since the long range mode index is weakly confined to the metal. The dominance of the former mode is confirmed by our simulations, although we attribute this to the fact that the long range mode is not efficiently excited in the current scheme. This can be visualised by considering the tangential component of the E-field of the guided plasmonic slab mode which has the same sign at each metal interface in the symmetric mode and opposite signs in the long range mode. With a plane wave excitation scheme as in our study (and presumably as will be implemented in practice), this requires the imposed field to have a similar distribution, that is, same sign for the symmetric mode, and opposite signs for the long range mode. When the metal is thin with respect to the wavelength, the imposed field at each side of the metal is almost identical and hence only the first mode is efficiently excited. Following [18], the mode index n_{SPP}, of the propagating wave can be approximated by

$$n_{SPP} = \sqrt{\left(\varepsilon_d + 4\varepsilon_d^{\,2} / k_0^{\,2} t^2 \varepsilon_m^{\,2}\right)}. \quad (1)$$

Here, ε_d and ε_m represent the relative permittivities of the surrounding dielectric and the metal, t denotes the thickness of the metal, and $k_0 = 2\pi/\lambda_0$ is the free space propagation constant. The mode index, n_{SPP}, is related to the propagation constant of the plasmon, $\beta_{SPP} = 2\pi/\lambda_{SPP}$, by $n_{SPP} = \beta_{SPP}/k_0$. Assuming a free space wavelength $\lambda_0 = 850$ nm, $\varepsilon_d = 1.51^2$, $\varepsilon_m = -27.9 - 1.9j$, and a metal thickness $t = 5$ nm, n_{SPP} is calculated to be $4.7 - 0.3j$ leading to $\lambda_{SPP} =$

#195436 - $15.00 USD Received 7 Aug 2013; revised 13 Sep 2013; accepted 16 Sep 2013; published 22 Oct 2013

182 nm. Therefore, the first order resonance in the finite strip should occur at $L = \lambda_{SPP}/2 = 91$ nm. However, additional phase picked up at the ends of the strip [18] reduces that length slightly so that λ_{SPP} is not equal to λ_{eff}. Furthermore, the introduction of feed gaps also affects λ_{eff}. In the rest of this work, λ_{eff} is determined numerically using λ_{SPP} as a starting point.

The proposed optical resonators are studied in a 2D geometry using frequency domain finite element analysis (FEA) implemented in Comsol Multiphysics [19]. The IMI structure is excited by a plane wave, with the E-field oriented along the length of the metallic bar in the transverse magnetic (TM) polarisation. The corners of the metallic segments are rounded by 0.5 nm for numerical stability and periodic boundary conditions are used to absorb the scattered waves. A computational domain of width (= period) of 500 nm and height of 700 nm is used throughout except for Fig. 7(b) of Section 3 where the width is increased to 1000 nm due to the large width of the device. At these widths, no field coupling between the individual antennas is observed, and to confirm this we have increased the period from 500 nm to 1000 nm. The result is a small drop (13%) in the amplitude of the resonance peak, which indicates that diffractive coupling [20] has a negligible effect on the antenna in this configuration. The incident free space wavelength and the material parameters listed above are used, and resonance is monitored by computing the maximum field enhancement, $|E_{max}/E_0|$, at the hot-spots in the dielectric surrounding the metallic resonator. These hot-spots are typically located at the feed gaps or the outer edges of the metal with the peak field enhancement at one of the corners of the metal. The particular corner yielding the peak field varies depending on the field distribution, which varies with resonator length, L. $|E_{max}/E_0|$ is extracted by scanning through these regions and finding the maximum value of $|E/E_0|$.

Dipole antenna with a single central feed gap

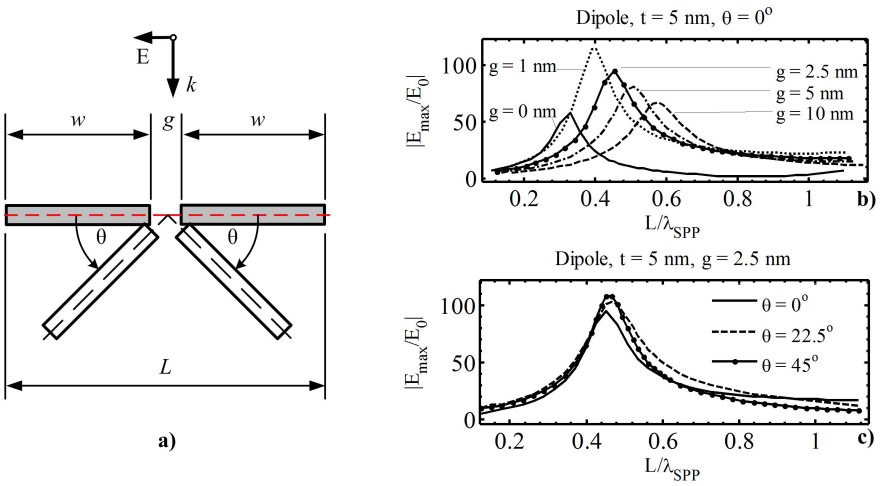

Fig. 2. a) Folded dipole antenna and its resonance as a function of L/λ_{SPP} at b) different feed gaps, g and at c) different fold angles, θ.

Optical dipole resonators of length L consisting of two feed arms separated by a feed gap (g), as illustrated in Fig. 2(a), are studied by varying the feed arm length (w) and monitoring plasmonic resonances. The metal thickness is t = 5 nm, the feed gap g is varied and the material parameters described above are used. The peak field enhancement, $|E_{max}/E_0|$, located at the corners of the metallic slabs in the feed gap (except for g = 0 nm, where the peak field occurs at the corners at the ends of the metal), is plotted as a function of L/λ_{SPP} for different values of g in Fig. 2(b). When g = 0 nm, a dipole resonance is excited for a metal length L = 60 nm, which is less than $\lambda_{SPP}/2$ = 91 nm due to the additional phase acquired at the ends of the metal. As g is increased, the maximum field enhancement initially increases since the feed gap provides access to the region of highest field while the resonant length increases,

#195436 - $15.00 USD Received 7 Aug 2013; revised 13 Sep 2013; accepted 16 Sep 2013; published 22 Oct 2013

indicating a red-shift in the resonance. For wider feed gaps, e.g. $g \geq 5$ nm, the resonance weakens as the perturbation gets significant. As we show here, the antenna still resonates when the two feed arms are folded towards each other by an angle 2θ and this is a key result of this paper (Fig. 2(a) and Fig. 2(c)). The resonant lengths remain almost unchanged at L ≈82.5 nm irrespective of the angle whilst the peak field in the folded case increases by ~15% compared to the case of θ = 0°.

A further interesting feature is observed in terms of additional modes supported by the resonator when the incident wave is rotated such that the E-field is now tilted by 45° to the horizontal. This is illustrated in Fig. 3(a) where the resonance of the unfolded dipole (θ = 0°) under normal and oblique incidence is plotted for different gap widths. Considering the case of g = 2.5 nm and θ = 0°, the first resonance occurs at the same length L = 82.5 nm for both normal and oblique incidence but the peak field enhancement is reduced by 30%. A second resonance is also observed at L ≈147.5 nm and 2D maps of the E-field for L = 82.5 nm and L = 147.5 nm for g = 2.5 nm are shown in Fig. 3(b) and Fig. 3(c). Clearly, the first peak corresponds to the first order resonant mode (m = 1), whilst the second corresponds to m = 2. With a normal incident field, only odd modes (m = 1, 3, 5…) are excited by symmetry. However, with an oblique excitation, both odd and even (m = 2, 4, 6…) modes are excited.

The standing field patterns in the metal for both modes are shown in Fig. 3(d) as the normalised field, $|E/E_0|$, as a function of x/L. $|E/E_0|$ is computed at the central axis of the dipole as indicated by the dashed line in Fig. 2(a). The different value of $|E/E_0|$ at x/L = 0 in each case is due to the different location of the gap; for m = 1, the gap is located at the region of maximum field in the metal, whilst for m = 2, the gap is at the node where the field tends to zero.

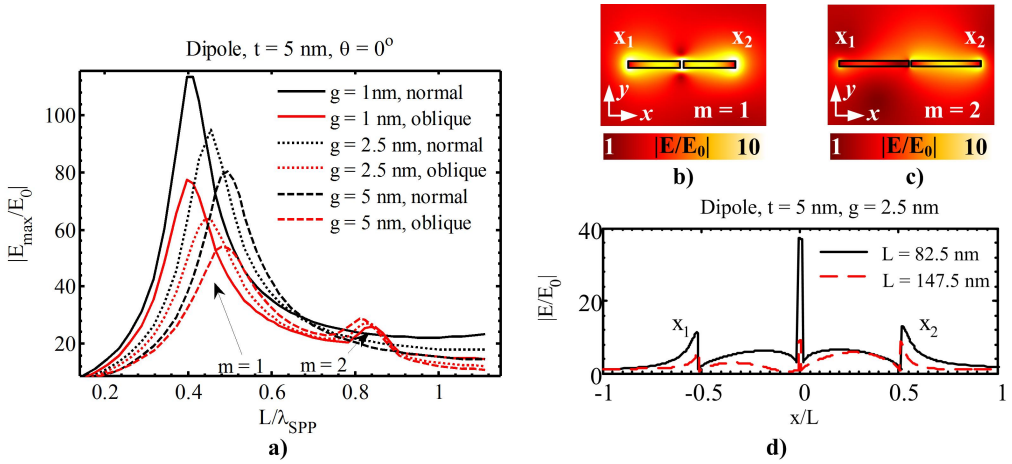

Fig. 3. a) $|E_{max}/E_0|$ as a function of L/λ_{SPP} for different feed gaps and excitations. E-field map for b) m = 1 and c) m = 2 at oblique incidence for g = 2.5 nm. d) $|E/E_0|$ on the metal highlighting the two modes. The x-axis is normalised to the respective value of L. In b) and c), the upper limit of the colour scale is restricted to 10 for clarity; $|E/E_0|$ values much greater than 10 are in fact obtained.

Dipole with two feed gaps

In practice, as indicated by the process flow of Fig. 1(b), the folded half wave antennas are realised as dolmen structures. In this context, the dolmen resonator consists of a horizontal segment (length = w_h) supported by two vertical segments (length = w_v) and separated by two feed gaps (width = g). The operation of such a structure is studied by considering a flat dipole segmented into three equal parts with two feed gaps, as illustrated in Fig. 4(a), and gradually folding the outermost arms until θ = 90° to obtain a dolmen. This resonator is excited by a normal TM plane wave with the E-field aligned to the horizontal. The variation of peak field

#195436 - $15.00 USD Received 7 Aug 2013; revised 13 Sep 2013; accepted 16 Sep 2013; published 22 Oct 2013

enhancement, $|E_{max}/E_0|$, with L/λ_{SPP} is shown in Fig. 4(b) at different fold angles for the case where $w_h = w_v$. The peak field enhancement is largest for θ = 45° but both folded arrangements (θ = 45° and θ = 90°) exhibit stronger resonances than the flat case (θ = 0°). In addition, the behaviour of the dolmen (θ = 90°) is investigated with oblique excitation. In this configuration, a second resonance is observed at L = 195 nm, corresponding to $m \approx 2$, and for the rest of this paper, this oblique incidence is adopted.

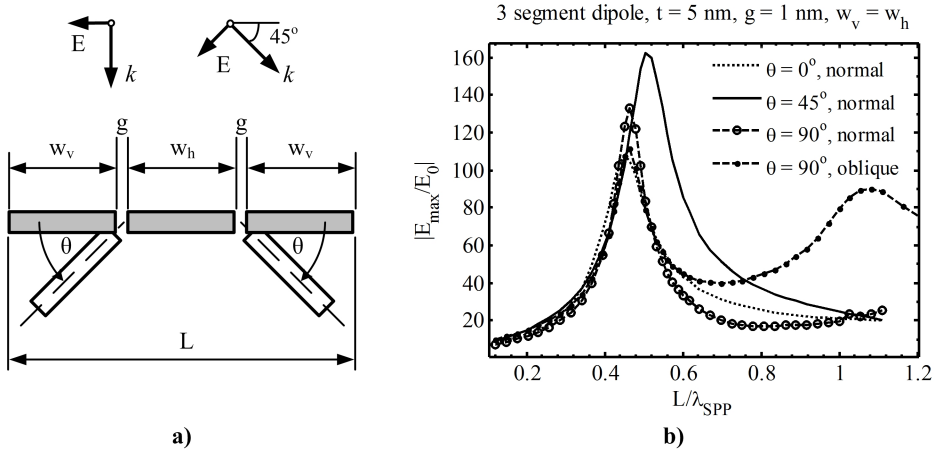

Fig. 4. a) Illustration of a three segment folded dipole with two feed gaps. The two outer arms are folded by an angle θ. b) Resonances of the three segment dipole at different fold angles, θ, and at normal or oblique incidence.

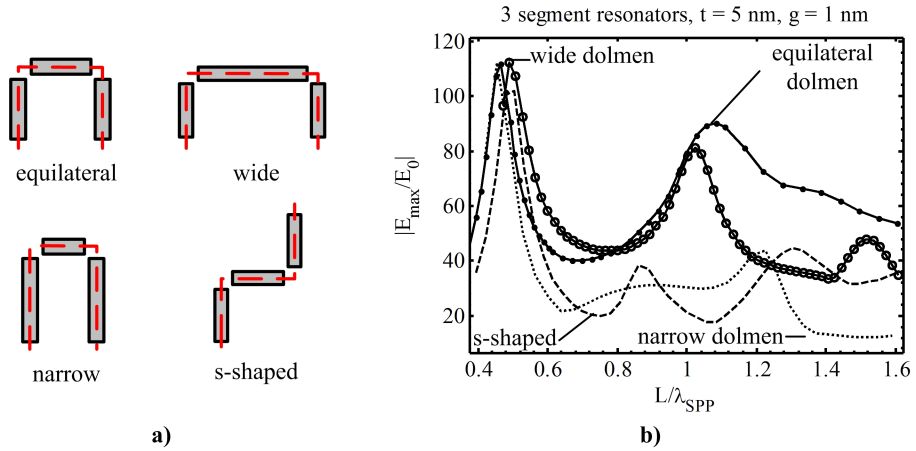

Fig. 5. a) The geometries derived from the 3 segment resonator and b) their resonances. The dashed lines (–) in a) correspond to the central axis of the metal.

The folded 3-segment antenna can lead to a number of configurations such as the equilateral dolmen considered above ($w_h = w_v$), scalene variations such as wide ($w_h > w_v$) or narrow ($w_v > w_h$), and sigmoid or s-shaped regular dolmen with both outer arms folded counter-clockwise by θ = 90° and $w_h = w_v$. These geometries are illustrated in Fig. 5(a) and their resonances are shown in Fig. 5(b) as a plot of $|E_{max}/E_0|$ as a function of L/λ_{SPP} under oblique excitation.

#195436 - $15.00 USD Received 7 Aug 2013; revised 13 Sep 2013; accepted 16 Sep 2013; published 22 Oct 2013

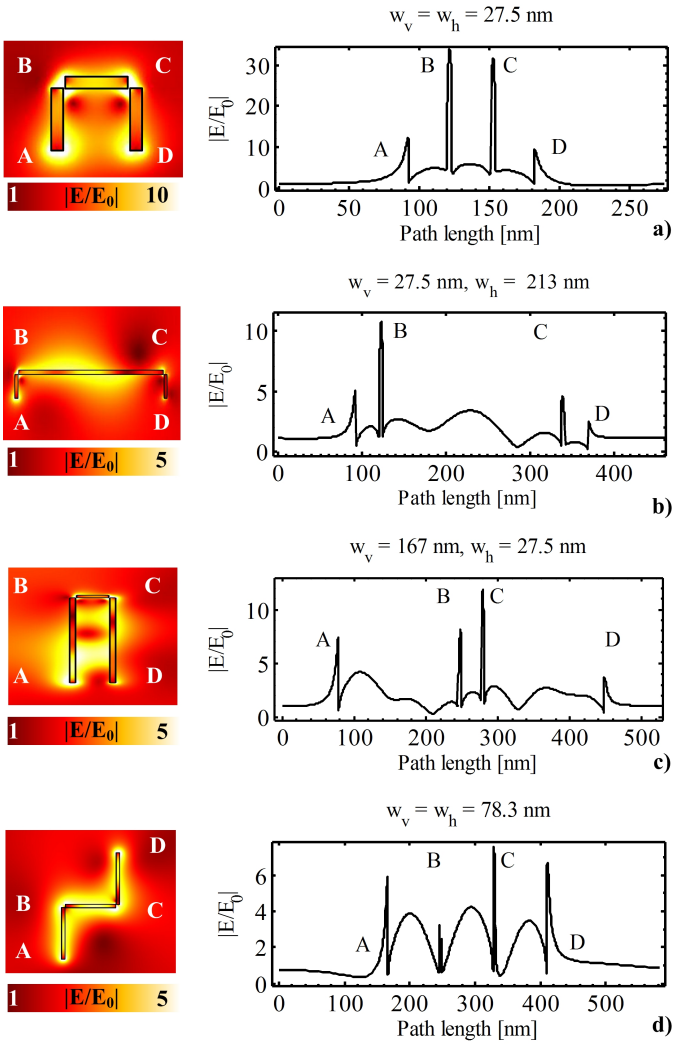

Fig. 6. E-field enhancement map and standing wave profile of the three segment resonator for a) equilateral dolmen resonator with L = 82.5 nm, b) wide dolmen with L = 270 nm, c) narrow dolmen with L = 364 nm, d) s-shaped or sigmoid resonator with L = 237 nm. The $|E/E_0|$ colour scales in the 2d maps are limited to 10 for a) and 5 for b), c), and d), for clarity. The path length in the standing wave profile corresponds to the dashed line (- -) in Fig. 5(a).

For the equilateral and wide dolmens, resonances are observed whenever $L \approx m\ \lambda_{SPP}/2$, where $L = w_h + 2(w_v + g)$, with the lower order resonances exhibiting stronger enhancements than the higher order ones due to losses accumulated over longer lengths. A 2d map of the E-field enhancement and the corresponding standing wave pattern along the middle of the metal (denoted by the dashed line in Fig. 5(a)) is shown for the m = 1 mode of the equilateral dolmen in Fig. 6(a)). Here, the half-wave mode field is equally distributed over the three segments and both feed gaps exhibit large E-field amplifications. An interesting feature of the equilateral dolmen is that no enhancement peak is observed for $m \approx 3$. This is attributed to the field distribution in the metal. Essentially, each metal segment supports a $\lambda_{SPP}/2$ mode with vanishing fields at its ends, such that the feed gaps, which are normally the regions of highest enhancement, are now at the zero-crossings of the standing wave. By the same argument, higher order modes which are multiples of m = 3 would also exhibit weak enhancements.

#195436 - $15.00 USD Received 7 Aug 2013; revised 13 Sep 2013; accepted 16 Sep 2013; published 22 Oct 2013

For the wide dolmen, w_v is set to 27.5 nm (which is $\approx L/3$ when $m = 1$) and w_h is varied and resonances are again observed when $L \approx m\ \lambda_{SPP}/2$, indicating that the mode described by Eq. (1) still dominates. The field enhancement map and the mode pattern on the metal for $m \approx 3$ are shown in Fig. 6(b). An interesting difference in the resonant behaviour between the equilateral dolmen and the wide dolmen occurs when the value of L/λ_{SPP} corresponds to $m \approx 3$ (see Fig. 5(b)). In the latter, the gaps are not located at the zero crossings, and hence a distinct resonance peak is observed.

In the narrow dolmen, w_h is set to 27.5 nm and w_v is varied. In this case, except for $m = 1$ which effectively represents the equilateral dolmen, the observed resonances do not correspond to $m = 2$ or $m = 3$. This is because the fields in the two vertical segments interact with each other due to their proximity. Effectively, this dolmen behaves as a lossy cavity as illustrated in the 2d field map (Fig. 6(c)). Similarly, the field on the metal does not show clear standing waves.

Lastly, the sigmoid or s-shaped resonator is considered. Here $w_h = w_v$ and a number of resonances are observed. The peak field enhancement for the first resonance is comparable to the other resonators and also occurs at the same value of L/λ_{SPP}. The higher order resonances however, occur at smaller resonator lengths compared to, e.g., the wide dolmen. We postulate that the phase shift acquired at each feed gap is now different compared to the dolmen due to the orientation of the vertical arms, thus resulting in different resonant lengths. The third resonance is illustrated in Fig. 6(d), showing the even distribution of the E-field over the entire resonator.

In this section, it has been shown that optical dipole antennas resonate even as their feed arms are rotated, and this is a key contribution of this work. As long as the dominant mode is the symmetric plasmonic IMI mode (as it is in all of the structures above except the narrow dolmen) and neglecting the phase shift due to reflection at the ends of the metal segments, resonance occurs when $L = m\lambda_{SPP}/2$. Also, the orientation of the feed arms with respect to the imposed field determines how efficiently the different modes are excited.

3. Wide dolmen resonator

The wide dolmen resonator (Fig. 7(a)) is now studied further due to its experimental relevance since w_v and w_h are defined by different processes (see Fig. 1). The additional degree of design freedom also allows different boundary conditions to be imposed, and an example is to set w_v to $\lambda_{SPP}/4 = 42$ nm to access the maximum field in the metal at the feed gaps. The field enhancement variation with L/λ_{SPP} is shown in Fig. 7(b). Compared to the case of $w_v = 27.5$ nm, the $w_v = \lambda_{SPP}/4 = 42$ nm case exhibits slightly higher field enhancements for high order resonances, and this is attributed to the fact that the field amplitude in the metal at $w_v = \lambda_{SPP}/3$ and $w_v = \lambda_{SPP}/4$ are similar. In fact, as observed by [18], introducing gaps at the regions of higher field in the metal can be more disruptive.

Far field spectrum

Another property of experimental relevance is the variation of far field parameters such as transmittance and reflectance with excitation wavelength, which can be used to monitor resonances. To model the frequency dependence of the optical properties of the metallic layer, a Drude model is used. The relative dielectric constant is defined by $\varepsilon_{rm} = \varepsilon_{r\infty} - \omega_p^2/\ \omega\ (\omega - j\omega_\tau)$. Here, $\varepsilon_{r\infty}$ is the high frequency dielectric constant, ω_p is the plasma frequency of the electron cloud, ω is the excitation frequency, and ω_τ is the damping frequency. From [21], $\varepsilon_{r\infty} = 9.07$, $\omega_p = 13.5 \times 10^{15}$ rads^{-1}, $\omega_\tau = 0.115 \times 10^{15}$ rads^{-1} for Au. The geometry corresponding to $m \approx 2$ with $w_v = 42$ nm and $w_h = 126.7$ nm is then simulated to compute the total absorption ($|A|^2$), the specular reflection ($|R_0|^2$), and the specular transmission ($|T_0|^2$), as illustrated in Fig. 7(c). The absorption spectrum is computed by subtracting the transmitted and reflected power densities by all diffraction orders from the injected power and clearly shows resonance at 850 nm. A second smaller peak is also observed at $\lambda_0 = 735$ nm, presumably corresponding to a

#195436 - $15.00 USD Received 7 Aug 2013; revised 13 Sep 2013; accepted 16 Sep 2013; published 22 Oct 2013

high order mode for a shorter excitation wavelength. However, the specular parameters, which are experimentally more accessible, only exhibit shallow peaks and dips.

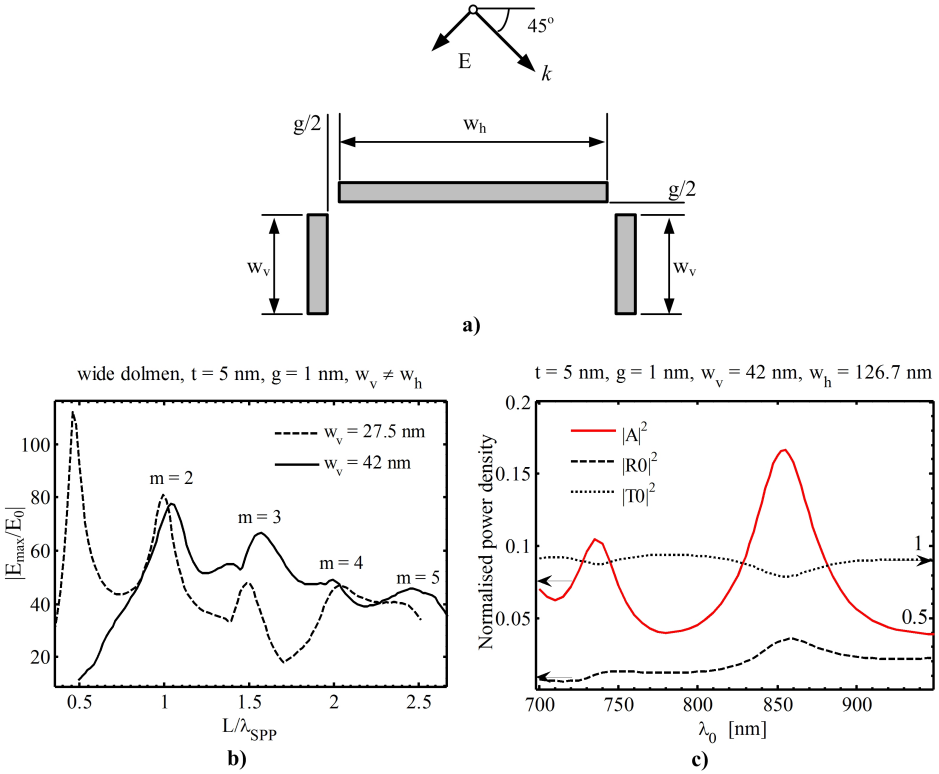

Fig. 7. a) Illustration of the wide dolmen under oblique illumination. b) Resonances of the wide dolmen with w_v = 27.5 nm and w_v = 42 nm. c) Spectrum of the resonator with L = 213 nm (m = 2).

Effect of adhesion layers

Adhesion layers such as Cr or Ti are usually required to stabilise Au layers on a supporting substrate. However, they also severely deteriorate the plasmonic resonance because they are typically very lossy. For example, at λ_0 = 850 nm, Cr has a relative dielectric permittivity of $-1.7 - 22.7j$. To quantify the losses, a Cr layer of variable thickness was added to the dolmen structure of Fig. 7(a), and the peak field enhancement is computed as a function of normalised resonator length (Fig. 8(a)). A significant drop in the peak field is observed as well as a slight red shift. Both effects increase as the Cr thickness is increased, the latter being probably due to the resulting increase in the feed gap. To minimise this effect, the technique employed in [22], where no adhesion layer is included near the hot-spots of the resonator, could be used. Alternatively, the adhesion layer could be avoided completely at the expense of mechanical stability.

Effect of unequal metal thickness

A consequence of the fabrication process is that the horizontal metal covered regions are subjected to ion bombardment whilst the vertical sidewalls are not (see Fig. 1(a)). Hence, the metallic IMI waveguide at the top of the dolmen may be thinner than the sides, and thus support different modes. The effect of the modal mismatch between the different segments of the waveguide is quantified by studying the model structure of Fig. 7(a) with w_v = 27.5 nm and varying w_h with different metal thicknesses. Here, the metal thickness of the vertical segments t_v is 5 nm and the thickness of the horizontal segment t_h is set to be a fraction of t_v.

#195436 - $15.00 USD Received 7 Aug 2013; revised 13 Sep 2013; accepted 16 Sep 2013; published 22 Oct 2013

The field enhancement is computed in each case to verify the shift in resonance and the results are illustrated in Fig. 8(b). The peak field enhancement, $|E_{max}/E_0|$, drops significantly as t_h is reduced due to a less efficient transfer of energy between the different metal segments. Also, as t_v is reduced, the value of n_{SPP} (see Eq. (1)) and λ_{SPP} decreases such thus explaining the left shift of the resonances in Fig. 8(b).

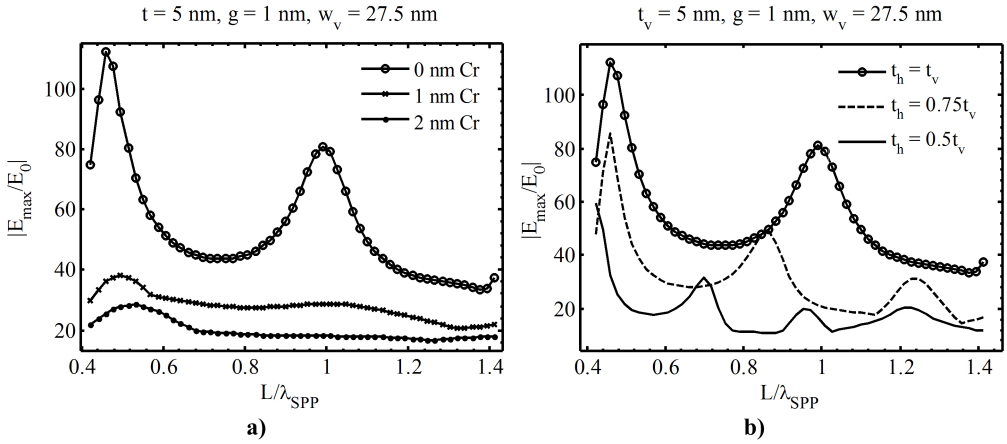

Fig. 8. a) Effect of a Cr adhesion layer illustrated by a shift in the resonant length as well as a significant weakening of the field enhancement, especially for higher orders. b) Effect of asymmetric metal thicknesses revealing a decrease in resonant length with a weakening of the field enhancement.

4. Conclusions

In this work, folded dipole and dolmen plasmonic resonators with feed gaps designed to operate at λ_0 = 850 nm have been proposed and studied by FEA. It is shown that these antennas exhibit discrete and strong resonances similar to their unfolded counterparts. The development of this antenna topology is motivated by the fact that parallel fabrication processes based on sidewall processing and ion beam edge structuring can generate such nano-antennas reliably over a very large scale. Also, the proposed geometry is, to the authors' knowledge, the first plasmonic resonator based on IMI slab waveguides that involves both in-plane and out-of-plane functional elements. The proposed fabrication process is particularly suited to 2D antennas. However, it could be extended to the third dimension to generate 'whispering gallery' like resonators with a dolmen cross section. Alternatively, assuming a nanometre scale 3D mesa as a starting point, the corner etching process would result in a metallic shell (formed by the 4 walls) and supporting a metallic cap. If both the cap and the shell resonate in tune, interesting effects could be obtained. The resonant behaviour will be different in both cases but potentially useful.

Large field amplitude enhancements of the order of 10^2 can be obtained at the feed gaps, and these can be used to enhance light-matter interactions. For example, in a recent work [23], this enhanced field (up to ~10 field amplitude enhancement) has been used for fluorescence analysis of single molecules at micro-molar concentrations. However, the antenna fabrication relied on FIB and was limited in area. Our proposed dolmen antenna topology provides field enhancement at hot-spots over a large area (essentially wafer scale) and therefore makes an optical antenna platform accessible for further studies of such nanoscale interactions. Future work will focus on the development and optimisation of the fabrication process and the experimental characterisation of the folded dipole resonators.

Acknowledgments

The authors would like to thank Prof. Mino Green for fruitful discussions and valuable input. This work was financially supported by The Leverhulme Trust (F/07 058/BR).

#195436 - $15.00 USD Received 7 Aug 2013; revised 13 Sep 2013; accepted 16 Sep 2013; published 22 Oct 2013